European Congress on Computational Methods in Applied Sciences and Engineering
ECCOMAS 2004
P. Neittaanmäki, T. Rossi, K. Majava, and O. Pironneau (eds.)
W. Rodi and P. Le Quéré (assoc. eds.)
Jyväskylä, 24–28 July 2004

COMPUTATIONAL MODELLING OF COMPLEX PHENOMENA IN BUBBLE DYNAMICS: VORTEX SHEDDING AND BUBBLE SWARMS

Heikki Haario*, Zhanna Korotkaya*, Pasi Luukka* and Anton Smolianski†

*Department of Information Technology
P.O. Box 20 , FIN-53851 Lappeenranta University of Technology, Finland
e-mail: heikki.haario@lut.fi

† Institute of Mathematics
CH-8057 Zurich University, Switzerland
e-mail: antsmol@amath.unizh.ch

Key words: CFD, Multiphase Flow, Bubble Dynamics, FEM, Level-Set, Operator-Splitting

Abstract. *We consider the direct numerical simulation of gas bubbles in viscous fluid flows. The behaviour of single bubbles and bubble swarms is studied with the particular emphasis on the bubble coalescence and breakage phenomena. For single bubbles, we are able to simulate the bubble dynamics in all relevant flow regimes, including the von Karman type vortex shedding and wobbling-bubble regime at high Reynolds number.*

Mathematically, our model is a combination of the Navier-Stokes equations and a free boundary problem for the bubble shape. The bubble boundaries are treated by the level set method that naturally allows the topology changes due to bubble coalescence and breakup. This, in addition to the simple finite-element method implemented in the operator-splitting framework, has proved to permit an accurate prediction of flows with moving interfaces in a wide range of physical parameters.

While the coalescence of bubbles in different flow regimes presents a very complicated phenomenon, the complex geometry of the physical domain brings some additional effects influencing the coalescence process. We present the numerical results illustrating the dynamics of two bubbles rising in a curvilinear cylinder in the ellipsoidal-shape flow regime.

1 INTRODUCTION

Two-phase flows, as a particular case of multi-phase flows, exhibit many complex physical phenomena, among which the interaction of gas bubbles in a viscous liquid plays a prominent role. The prediction and understanding of the processes of the coalescence and breakup of single bubbles as well as bubble swarms is extremely important for the comprehensive analysis of bubbly flows, particularly, for the evaluation of such quantities as total interfacial area, mass transfer rate and gas slip velocity. However, a detailed study of bubbly flows becomes fairly incomplete without gaining an insight into the phenomenon of motion of a single bubble or a small group of bubbles. The computational investigation of this phenomenon constitutes a primary goal of the present work. This is a continuation of our previous research on the dynamics of a single gas bubble rising in a viscous liquid (see [1]) and the same, finite-element/level-set/operator-splitting method that was proposed in [2] is used in this study. The numerical method allows to simulate a wide range of flow regimes, to accurately capture the shape of the deforming interface of the bubble and the surface tension effect, while maintaining a good mass conservation.

Using the proposed computational method we can systematically study diverse flow regimes for a single buoyant bubble and bubbles swarms in different geometries. Unfortunately, due to the highly unstable and small-scale nature of the considered problems there are very few experimental investigations, but the comparison with available experimental data confirms a good accuracy of our numerical predictions. In this work, we present the results on the helical vortex path behind a single buoyant bubble and the simulations of a bubble swarm in a simple geometry as well as the coalescence of two bubbles in a more complex geometry.

The rest of the paper is organized as follows. The mathematical model for unsteady viscous flow of two immiscible fluids is discussed in Section 2. In the same section, the computational approach is presented. Section 3 is devoted to the numerical experiments and some conclusions are drawn in Section 4.

2 MATHEMATICAL MODEL AND COMPUTATIONAL METHOD

In the paper an unsteady laminar flow of two immiscible fluids is considered. Both fluids are assumed to be incompressible viscous and Newtonian in absence of any surfactants. It is supposed that the flow is isothermal to avoid variations of viscosity and density due to changes of a temperature field. The validity of this assumption is affected by several factors, the most important of which is the condition for Mach number to be smaller than, approximately, 1/3 (see [3] for a thorough discussion on the incompressibility assumption). That condition is satisfied in our case, since we deal with essentially subsonic flows. Presuming, in addition, the fluids to be homogeneous, we may infer that the densities and viscosities are constant within each fluid. We utilize the sharp-interface (zero interfacial thickness) approach; the density and viscosity have, therefore, a jump discontinuity at the interface (see, e.g., [3]). We assume that the interface has a surface tension. It is

supposed also that there is no mass transfer through the interface (i.e. the interface is impermeable), and there are no surfactants present in the fluids (hence, there is no species transport along the interface). Under such conditions there is no need to consider the variations of surface tension coefficient in tangential to the interface direction, i.e. the solutocapillary Marangoni effect (the thermocapillary Marangoni effect has been excluded by the assumption on isothermal character of the flow). Therefore, the surface tension coefficient may be assumed constant.

Suppose that the motion of two viscous immiscible fluids under our investigation is confined to some closed domain. The boundary of the domain can be physical (e.g., the walls of a container), artificial (if we consider a flow in unbounded domain) or partly artificial. In fact, we can always restrict ourselves to some bounded region of interest and consider, then, the flow in that region only. On the other hand, this enables us to avoid dealing with asymptotics at infinity and to make the problem more tractable from computational viewpoint. Let us denote the boundary of the domain by Σ, the domains occupied with the fluids by Ω_1 and Ω_2 and the interface between the fluids by Γ ($\Gamma = \partial\Omega_1 \cap \partial\Omega_2$, where $\partial\Omega_i$ is the boundary of $\Omega_i, i = 1, 2$). Let also Ω be the entire region occupied with the fluids, i.e. the interior of the domain ($\Omega = \Omega_1 \cup \Omega_2 \cup \Gamma$). The domains Ω_1 and Ω_2 may be multiply connected, and the interface Γ may intersect the region boundary Σ.

Taking into account the physical assumptions considered above, we may assert that the flow of both fluids is governed by the incompressible Navier-Stokes equations

$$\rho(\mathbf{x})\left(\frac{\partial \mathbf{v}}{\partial t} + \mathbf{v}\cdot\nabla\mathbf{v}\right) - \nabla\cdot(2\mu(\mathbf{x})\underline{\underline{\mathbf{S}}}) + \nabla p = \rho(\mathbf{x})\mathbf{g}\,, \tag{1}$$

$$\nabla\cdot\mathbf{v} = 0 \qquad \text{in } \Omega\,,\ t > 0 \tag{2}$$

supplemented with the interfacial conditions

$$[\mathbf{v}]|_\Gamma = 0\,, \quad [-p\underline{\underline{\mathbf{I}}} + 2\mu\underline{\underline{\mathbf{S}}}]|_\Gamma \cdot \mathbf{n} = \kappa\sigma\mathbf{n}\,. \tag{3}$$

Here the density $\rho(\mathbf{x}) = \rho_1$ in Ω_1 and ρ_2 in Ω_2, the viscosity $\mu(\mathbf{x}) = \mu_1$ in Ω_1 and μ_2 in Ω_2, $\mathbf{g}$ is the acceleration of gravitational field, $\underline{\underline{\mathbf{S}}} = \frac{1}{2}(\nabla\mathbf{v} + (\nabla\mathbf{v})^T)$ is the deformation rate tensor, $\underline{\underline{\mathbf{I}}}$ is the identity tensor, σ is the coefficient of surface tension, κ is twice the mean curvature of the interface, $\mathbf{n}$ is the unit normal to the interface, and $[...]|_\Gamma$ denotes a jump across the interface Γ.

The equations (1)–(2) and interfacial conditions (3) should be complemented with some boundary condition on Σ for velocity (it is addressed in Section 3) and with the initial conditions

$$\Gamma|_{t=0} = \Gamma^{(0)} \tag{4}$$

$$\mathbf{v}|_{t=0} = \mathbf{v}^{(0)} \quad \text{in } \Omega^{(0)}\,, \tag{5}$$

where $\Gamma^{(0)}$ is the initial position of the interface determining initial shapes of the domains $\Omega_1^{(0)}$ and $\Omega_2^{(0)}$.

Obviously, there are three unknowns here: the velocity of fluid $\mathbf{v}(\mathbf{x},t)$, the pressure $p(\mathbf{x},t)$ and the interface $\Gamma(\mathbf{x},t)$. The position of the interface at any moment of time can be determined using the fact that, in the absence of mass transfer through the interface (see the first of the interfacial conditions (3)), the interface is convected by the fluid, i.e. the interface normal velocity is equal to the normal component of fluid velocity (the latter is continuous across the interface, see (3)).

The problem at hand contains three key ingredients: (i) flow equations (i.e. the Navier-Stokes equations with discontinuous coefficients and singular capillary force), (ii) moving interface and (iii) coupling between velocity-pressure fields and the interface (through the coefficients, capillary force and interfacial advective velocity). To attack the problem numerically we advocate the operator-splitting approach; namely, at each time step, we first resolve the Navier-Stokes system with fixed known interface, then, using computed velocity field, we find the new approximation of the interface. Having found the new interface position we can calculate its normal and curvature, and, thus, evaluate the surface tension force and the density/viscosity coefficients to be used on the next time step in the Navier-Stokes equations.

2.1 Discretization of the Navier-Stokes equations

Using the Marchuk-Yanenko fractional-step scheme (see, e.g., [4]) we may separate the convective nonlinearity, viscous diffusion and incompressibility from one another and treat each of them with corresponding numerical technique. Thus, on each time interval $[t_n;t_{n+1}]$ the Navier-Stokes (NS) system (1)–(3) is approximated by a sequence of three subproblems:

1. NS-convection step
$$\frac{\partial \mathbf{v}}{\partial t} + \mathbf{v}\cdot\nabla\mathbf{v} = 0 \qquad \text{in } \Omega\times(t_n;t_{n+1})\,, \tag{6}$$
$$\mathbf{v}|_{t=t_n} = \mathbf{v}^n\,,$$
$$\Longrightarrow \mathbf{v}^*\,.$$
2. Viscous step
$$\rho(\mathbf{x})\frac{\partial \mathbf{v}}{\partial t} - \nabla\cdot(2\mu(\mathbf{x})\underline{\mathbf{S}}) = \rho(\mathbf{x})\mathbf{g} \quad \text{in } \Omega\times(t_n;t_{n+1})\,, \tag{7}$$
$$[\mathbf{v}]|_\Gamma = 0\,, \quad [2\mu\underline{\mathbf{S}}]|_\Gamma\cdot\mathbf{n} = \kappa\sigma\mathbf{n} \quad \text{on } \Gamma\,,$$
$$\mathbf{v}|_{t=t_n} = \mathbf{v}^*\,,$$
$$\Longrightarrow \mathbf{v}^{**}\,.$$
3. Projection step
$$\frac{\partial \mathbf{v}}{\partial t} + \frac{1}{\rho(\mathbf{x})}\nabla p = 0\,, \tag{8}$$
$$\nabla\cdot\mathbf{v} = 0 \qquad \text{in } \Omega\times(t_n;t_{n+1})\,,$$

$$
\begin{aligned}
&[\mathbf{v}]|_\Gamma \cdot \mathbf{n} = 0\,, \quad [p]|_\Gamma = 0 \quad \text{on } \Gamma\,,\\
&\mathbf{v}|_{t=t_n} = \mathbf{v}^{**}\,,\\
&\Longrightarrow \mathbf{v}^{n+1}\,,\ p^{n+1}\,.
\end{aligned}
$$

Here $\mathbf{v}^n(\mathbf{x})$ and $p^n(\mathbf{x})$ are the approximations to $\mathbf{v}(\mathbf{x}, t_n)$ and to $p(\mathbf{x}, t_n)$, $n = 0, 1, \ldots$, respectively, and $\mathbf{v}^0 \equiv \mathbf{v}^{(0)}$. Each of three subproblems must be complemented by suitable boundary conditions which will be discussed below. The general strategy consists in resolving the steps successively; moreover, each step can be treated with its own time discretization scheme employing a specific (variable) time-step size dictated by stability and/or accuracy reasons. Thus, the given global time step $\Delta t = t_{n+1} - t_n$ may be subdivided into smaller time steps within each of the subproblems.

The operator-splitting implies a decomposition of the interfacial conditions. The splitting of the interfacial stress jump condition indicates that the surface tension balances the jump of viscous stress only (subproblem 2), while the pressure is simply continuous across the interface (subproblem 3). Such approximation of the interfacial condition seems to be in contradiction with the fact that the pressure does have a jump discontinuity at the interface, which can be clearly seen from the famous Laplace-Young equation, if the viscosity is very small. However, the numerical tests indicate that the chosen scheme is capable of capturing the pressure interfacial discontinuity with a good accuracy; thus, there is no need to enforce the discontinuity explicitly (see the discussion in [2]).

All the subproblems (6)–(8) are discretized in space by the finite element method using a single uniform triangulation for both velocity and pressure. If we denote the triangulation by $\mathcal{T}_h$, where h is the mesh size (i.e. the maximal diameter of the triangles), the approximation space for the pressure can be defined as

$$
Q^h = \{p_h \in C^0(\overline{\Omega}) \Big|\, p_h|_T \in \mathbb{P}_1 \,\forall T \in \mathcal{T}_h\}\,, \tag{9}
$$

where $\mathbb{P}_1$ is the space of polynomials in two variables of degree less than or equal to 1. The discrete velocity belongs to the following space:

$$
\mathbf{V}^h = \{\mathbf{v}_h \in \mathbf{C}^0(\overline{\Omega}) \Big|\, \mathbf{v}_h|_T \in \mathbb{P}_* \times \mathbb{P}_* \,\forall T \in \mathcal{T}_h\}\,, \tag{10}
$$

where $\mathbb{P}_*$ is defined as (a) $\mathbb{P}_* \equiv \mathbb{P}_1$ or (b) $\mathbb{P}_* \equiv \mathbb{P}_1^b$ or (c) $\mathbb{P}_* \equiv \mathbb{P}_2$. Here $\mathbb{P}_1^b = \mathbb{P}_1 \bigoplus \mathrm{span}\{\lambda_1\lambda_2\lambda_3\}$ (λ_i , $i = 1, 2, 3$, are the area (barycentric) coordinates on the triangle T), and $\mathbb{P}_2$ is the space of polynomials in two variables of degree less than or equal to 2. In the case (a) we deal with the $\mathbb{P}_1/\mathbb{P}_1$ finite element for the velocity and pressure, in the case (b) with the so-called "mini" finite element, and in the case (c) with the "Taylor-Hood" finite element (see, e.g., [5]). It is worth noting that the "mini" and "Taylor-Hood" elements satisfy the LBB (*inf-sup*) condition, while the equal-order ($\mathbb{P}_1/\mathbb{P}_1$) approximation does not. However, in combination with the operator-splitting (7)–(8) (which is, in fact, a continuous version of the well-known Chorin projection scheme), the $\mathbb{P}_1/\mathbb{P}_1$ approximation is stable, if the time step $\Delta t \geq Ch^2$ (C is a constant), see, e.g., [6]. This

fact enables us to use the most economical but sufficiently accurate $\mathbb{P}_1/\mathbb{P}_1$ approximation for the velocity and pressure.

Now we address briefly the solution of the subproblems (6)–(8). The Navier-Stokes convection step is the first-order nonlinear hyperbolic problem, and, thus, the boundary conditions consist of prescribing the fluid velocity only on the inflow part of the boundary Σ (i.e. where the fluid velocity is directed inward the domain Ω). Then the problem is solved with the explicit Taylor-Galerkin scheme of [7].

The viscous step requires the boundary conditions to be as for the complete problem, i.e. (**??**). The use of the finite element method for spatial discretization of the viscous step is very essential, since in the weak (variational) formulation, on which the method relies, the interfacial stress jump condition becomes a *natural* condition. Thus, after multiplying (7) with weighting function $\mathbf{w}$ and integrating in Ω by parts, the surface tension force becomes automatically incorporated into the variational formulation:

$$\int_\Omega \rho(\mathbf{x})\frac{\partial \mathbf{v}}{\partial t}\cdot\mathbf{w}\,dx + \int_\Omega 2\mu(\mathbf{x})\underline{\underline{\mathbf{S}}}\cdot\cdot\nabla\mathbf{w}^T\,dx \;=\; \int_\Omega \rho(\mathbf{x})\mathbf{g}\cdot\mathbf{w}\,dx + \int_\Gamma \kappa\sigma\mathbf{n}\cdot\mathbf{w}\,d\Gamma\,. \quad (11)$$

The method does not require to approximate a delta-function as it is usually done for the accounting of singular capillary force (see, e.g., [8], [9]) and, hence, precludes the interface smearing. If the interface Γ can be localized "precisely" (i.e. with the accuracy of the discretization scheme), then a sharp interface may be maintained, and the error in the interface location may be expected to be of the order of the discretization error. Particularly, the second-order accuracy in space can be recovered with the piecewise linear interpolation of all variables (velocity, pressure, interface). Another advantage of the considered approach consists in alleviating the singularity connected with the differentiation of discontinuous viscosity coefficient; in fact, this problem is completely eliminated with the formulation (11).

After an implicit temporal discretization of (11) with the backward Euler or the Crank-Nicolson scheme, we obtain a linear algebraic system having symmetric and positive-definite matrix, which could be successfully solved, for instance, by incomplete Cholesky preconditioned conjugate gradient method.

The projection step defines an inviscid flow problem, thus, the boundary conditions consist in prescribing the boundary values only for the normal component of fluid velocity on Σ. After implicit time-discretization with the time step Δt the problem can be recast in the form of a Poisson-type equation for the pressure endowed with the homogeneous Neumann boundary condition

$$-\nabla\cdot\left(\frac{1}{\rho(\mathbf{x})}\nabla p^{n+1}\right) = -\frac{1}{\Delta t}\nabla\cdot\mathbf{v}^{**} \qquad \text{in } \Omega\,, \quad (12)$$

$$\mathbf{n}\cdot\nabla p^{n+1}|_\Sigma = 0\,, \quad (13)$$

where $\mathbf{v}^{**}$ is the intermediate velocity obtained on the viscous step. The final divergence-

free velocity $\mathbf{v}^{n+1}$ is then derived as

$$\mathbf{v}^{n+1} = \mathbf{v}^{**} - \Delta t \frac{1}{\rho(\mathbf{x})} \nabla p^{n+1} \,. \tag{14}$$

2.2 Approximation of the interface

We use the level-set approach (see [10], [11]) for capturing the interface Γ. The approach consists in specifying a continuous "level-set function" Φ such that Φ is the signed distance to the interface Γ, $\Phi > 0$ in Ω_2 and $\Phi < 0$ in Ω_1. Obviously, we have $\Gamma = \{\mathbf{x} |\, \Phi(\mathbf{x}, t) = 0 \; \forall t \geq 0\}$ and $|\nabla \Phi| = 1$ in Ω.

Since the interface is convected with the fluid velocity, the following evolution equation for $\Phi(\mathbf{x}, t)$ can be easily derived (see, e.g., [12]):

$$\frac{\partial \Phi}{\partial t} + \mathbf{v} \cdot \nabla \Phi = 0 \quad \text{in } \Omega \,,\; t > 0 \,. \tag{15}$$

We solve this pure advection equation with the fluid velocity $\mathbf{v}$ found as the solution of the Navier-Stokes system and with the same explicit Taylor-Galerkin scheme of Quartapelle & Selmin as on the Navier-Stokes convection step. The continuous piecewise-linear approximation is utilized for Φ on the same uniform grid that is used for velocity-pressure approximation. Such approximation allows easily localizing the interface at any moment of time: indeed, the intersection of the approximate level-set function with each triangle of the grid is just a line segment possibly degenerated to a point (a vertex of the triangle); moreover, to find this line segment one has to determine only the intersection points of the approximate, linear level-set function with triangle's edges. Thus, using piecewise linear continuous approximation for the level-set function on simplicial mesh, we obtain *unique* piecewise linear representation for the interface Γ.

At the beginning of computational process the level-set function Φ is initialized as the signed distance to the interface $\Gamma^{(0)}$. But, as time goes, the level-set function may become very steep or flat in some regions, particularly in the vicinity of the interface, thus losing the nice property $|\nabla \Phi| = 1$. This deterioration of the level-set function is a natural consequence of the convection process, but it makes difficult an accurate determination of the interface. In order to cure the situation, the level-set function must be *reinitialized*, i.e. made again the signed distance function. It is worthwhile to note that this "redistancing" should be done only in some vicinity of the interface, since the values of the level-set function far from Γ have no influence on the interface dynamics. Using the interface localization discussed above, the redistancing can be done by straightforward computation of the normal distance to the interface at each grid point located within the mh-band around the interface (integer m ranges typically between 5 and 10). The algorithm has a complexity $\mathcal{O}(N^2)$, where N is the number of grid nodes along one coordinate direction, i.e. depends linearly on the total number of grid points (see [2]).

The reinitialization of the level-set function is very important for accurate determining the interface, but it cannot guarantee the mass conservation. In fact, due to the

incompressibility assumption the area (volume in 3D) of the region occupied with each of the two fluids must be conserved during the whole computational process. However, this is not the case because of different numerical errors, and after many time-steps or any change of the interface topology the relative decrease/increase of the area of one of the fluids may be about several percents (see, e.g., [8]). We propose a very simple and efficient approach that uses an additional, *level-set correction* step to explicitly enforce the mass conservation. Suppose that we have performed the reinitialization of the level-set function Φ, thus, in some vicinity of the interface, Φ is the signed distance function and its level sets (isolines) are equidistant. Then we may easily correct the area of the domain $\Omega_2 = \{\mathbf{x} \in \Omega \,:\, \Phi > 0\}$, still retaining the shape of the interface, by considering as a new zero-level set some isoline of Φ that lies in the vicinity of the current interface curve. Mathematically, the procedure can be accomplished simply by letting $\Phi^{new} = \Phi + C_\Phi$, where the signed constant C_Φ is found from the expression

$$C_\Phi = \frac{S_{exact} - S(\Omega_2)}{L(\Gamma)}\,, \tag{16}$$

where $L(\Gamma)$ is the length of the interface Γ, S_{exact} is the exact area of the region occupied with the second fluid (S_{exact} is always known to us), $S(\Omega_2)$ is the area of Ω_2. The formula (16) is accurate up to $\mathcal{O}(C_\Phi^2)$ (we assume that $0 < l_1 \le L(\Gamma) \le l_2 < +\infty$, l_1 and l_2 are independent of any physical and numerical parameters of the problem).

We may note that the level-set correction procedure makes sense also in the case of multiply-connected domain Ω_2 and in the case when Γ is only a part of the boundary of Ω_2.

The justification of the level-set correction is essentially based on two facts: Φ being a distance function in some vicinity of the interface and smallness of $|C_\Phi|$. The former fact means that the level-set correction should follow the reinitialization on every time-step. The smallness of modulus of the correction constant is the crucial point in justifying the method; indeed, artificial moving of the interface is not allowed, except as the movement magnitude is not greater than the interface interpolation error. If we assume that $\Gamma \in C^2$, the piecewise linear interfacial interpolation gives us the error $\mathcal{O}(h^2)$. Hence, $|C_\Phi|$ should not be greater than $\mathcal{O}(h^2)$; in [2] it is shown to be so. It is worth noting that the effect of the level-set correction is usually almost negligible within one time-step, but the correction's main purpose is to prevent an accumulation of numerical errors in a long run.

Finally, if the piecewise-linear approximation is utilized for Φ, the total error of mass conservation is kept within $\mathcal{O}(h^2)$ accuracy of the interface approximation, and the level-set correction yields also an additional stabilization of the interface motion (see [2]).

2.3 Approximation of interface normal and curvature

Having computed the piecewise-linear approximation Φ_h of the level-set function, we can find the interface normal by virtue of the formula $\mathbf{n}_h = \nabla\Phi_h/|\nabla\Phi_h|$. This results in a piecewise-constant approximation of the normal; it is shown in [2] that applying

a standard gradient averaging procedure to $\mathbf{n}_h$ leads to the piecewise-linear continuous approximation $\tilde{\mathbf{n}}_h$ having $\mathcal{O}(h^2)$ accuracy. It is important that, since Φ_h is defined over the entire domain Ω, $\tilde{\mathbf{n}}_h(\mathbf{x})$ is also formally defined for almost every $\mathbf{x} \in \Omega$. Using this fact, we may compute the curvature by two methods: either directly as

$$\kappa_h = -\nabla \cdot \tilde{\mathbf{n}}_h \tag{17}$$

or by using the variational formulation for the curvature equation

$$\int_\Omega \tilde{\kappa}_h q_h \, dx = \int_\Omega \tilde{\mathbf{n}}_h \cdot \nabla q_h \, dx - \int_\Sigma (\tilde{\mathbf{n}}_h \cdot \mathbf{n}_\Sigma) q_h \, d\Sigma \,, \quad \tilde{\kappa}_h \in Q^h \,, \ \forall q_h \in Q^h \,, \tag{18}$$

where $\mathbf{n}_\Sigma$ is the outward unit normal to the boundary Σ and Q^h is the finite-dimensional space of continuous piecewise-linear functions defined on the considered uniform triangulation. Solution of (18) amounts simply to resolving the system with the consistent mass matrix. It is demonstrated in [2] that the piecewise-constant approximation κ_h has $\mathcal{O}(h)$ accuracy, while the piecewise-linear $\tilde{\kappa}_h$ attains the accuracy $\mathcal{O}(h^2)$. The latter fact is quite remarkable, since we use only *linear* interface approximation, and allows us to evaluate accurately the surface tension force.

2.4 Summary of the algorithm

Our computational approach for numerical modelling of interfacial flows can be summarized as follows:

Step 0. Initialization of the level-set function and velocity.

For each n-th time-step, $n = 1, 2, \ldots$:

1. Computation of interface normal and curvature.
2. Navier-Stokes convection step.
3. Viscous step.
4. Projection step.
5. Level-set convection step.
6. Reinitialization step.
7. Level-set correction step.

The steps 1.–7. are performed successively, and each of the steps 2.–5. may use its own local time-increment size. On each step the *last* computed velocity is exploited; the viscous and projection steps use the interface position found on the previous global time-step. It is also noteworthy that the steps 5.–7. of the n-th time-step can be computed in a fully parallel manner with the step 2. of the next, $(n+1)$-st time-step. The whole algorithm is very flexible; it permits, for instance, to compute unsteady interfacial Stokes flow just by omitting the Navier-Stokes convection step.

3 NUMERICAL EXPERIMENTS

3.1 Bubble rising in different shape regimes

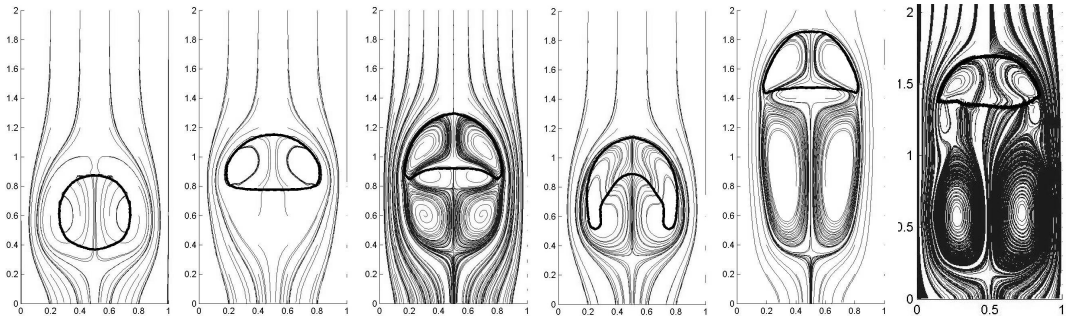

(a) (b) (c) (d) (e) (f)

Figure 1: Different computed shapes of bubbles: (a) spherical with Re=1, Eo=0.6, (b) ellipsoidal with Re=20 Eo=1.2, (c) dimpled ellipsoidal cap with Re=35, Eo=125, (d) skirted with Re=55, Eo=875, (e) spherical cap with Re=94, Eo=115 and (f) wobbling with Re=1100, Eo=3.0; $\rho_1/\rho_2 = 10^3$; $\mu_1/\mu_2 = 10^2$.

The typical bubble shapes and velocity streamlines in the frame of reference of the bubble are shown in Figure 1. Although all experimental results correspond to three-dimensional bubbles and our computations are two-dimensional, a qualitative comparison is possible. The comparison enables us to conclude that our numerical bubble shapes are in a good agreement with the experimental predictions of [13] and [14]. It is worth noting that all basic shapes are successfully recovered with the physical parameter values lying exactly within the limits given in [14].

3.2 Vortex shedding

Vortex shedding phenomena can be observed in different bubble flow regimes, but the case of a wobbling bubble exhibits the most pronounced unsymmetric vorticity pattern in the bubble wake and, at the same time, is the most difficult for numerical simulations owing to its notorious interface-instability. The wobbling typically appears with sufficiently high Reynolds numbers when the Eötvös number is, roughly, in the range between 1 and 100 (see [14]).

With Reynolds $Re = 900$ and Eötvös number $Eo = 20.2$, one can observe a pronounced wake instability (see Figure 2; in this simulation the liquid has the same properties as water but the gas is ten times more dense than air). While the wobbling of the bubble bottom remains apparent, the bubble top makes the bubble shape resemble a spherical cap. The remarkable bubble wake, known in the literature as the helical vortex path, is in a good qualitative agreement with experimental investigations of [15].

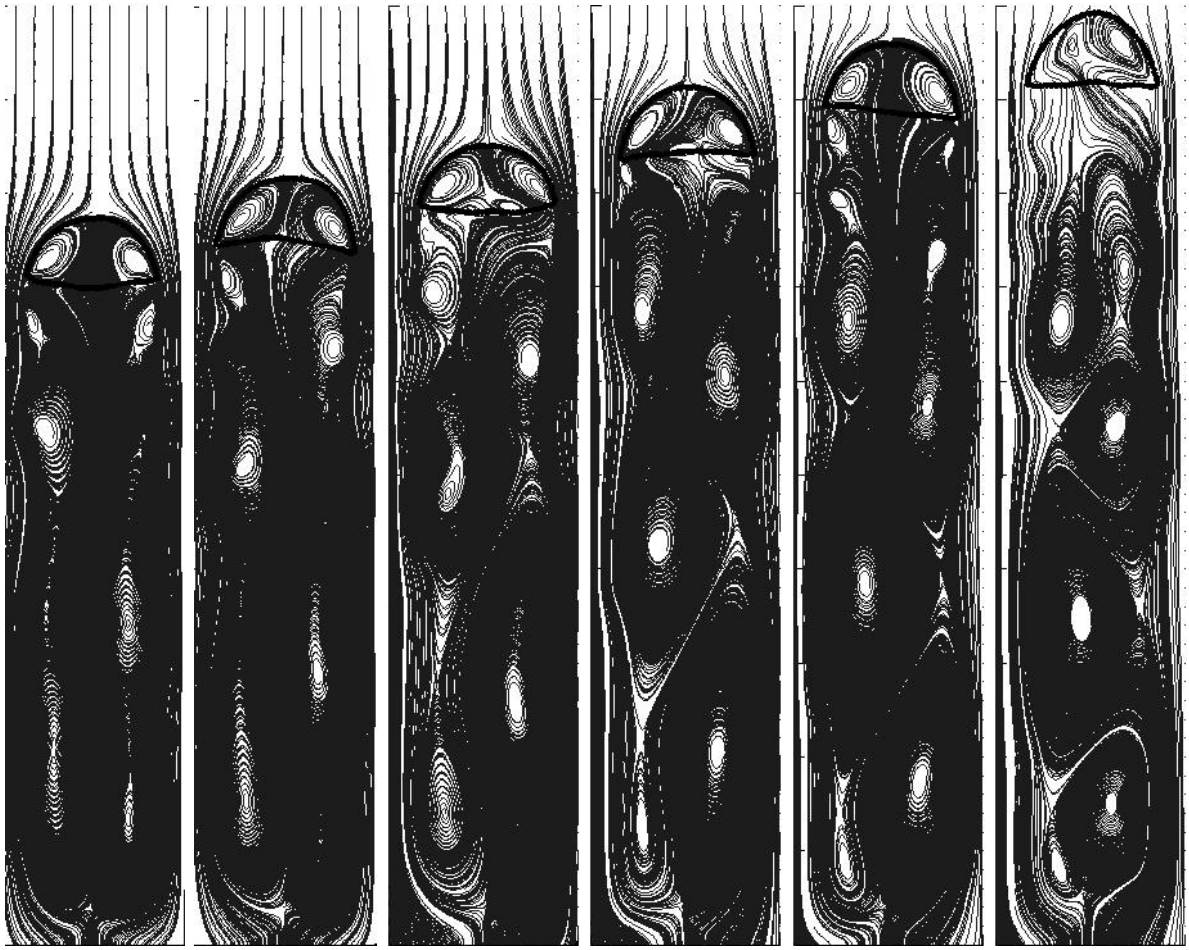

Figure 2: Helical vortex path behind the bubble. $Re = 900$, $Eo = 20.2$, $\mu_1/\mu_2 = 10$, $\rho_1/\rho_2 = 10^2$.

3.3 Interaction of bubbles in complex geometry

Here we demonstrate the results on the simulation of a merger of two bubbles in a 'wavy' cylindrical domain. We prescribe the free-slip velocity condition on the curvilinear walls of the cylinder, the no-slip condition on its bottom and the outflow condition on its top (the same boundary conditions for velocity were used in other numerical tests). Initially, the bubbles are circular with the same radius 0.25 and the same axis of symmetry.

The process of bubbles' rise and coalescence was investigated in the ellipsoidal-shape regime, and the corresponding results can be seen in Figures 3 – 4. The general behaviour of the bubbles is rather similar to their dynamics in the case of a rectangular geometry (see [**?**]), but the influence of the curvilinear walls manifests itself in the multiple vortices occuring at different parts of the domain. This geometry-generated vorticity dominates the vortices forming in the bubbles' wake and creates a highly unsteady non-symmetric

flow pattern.

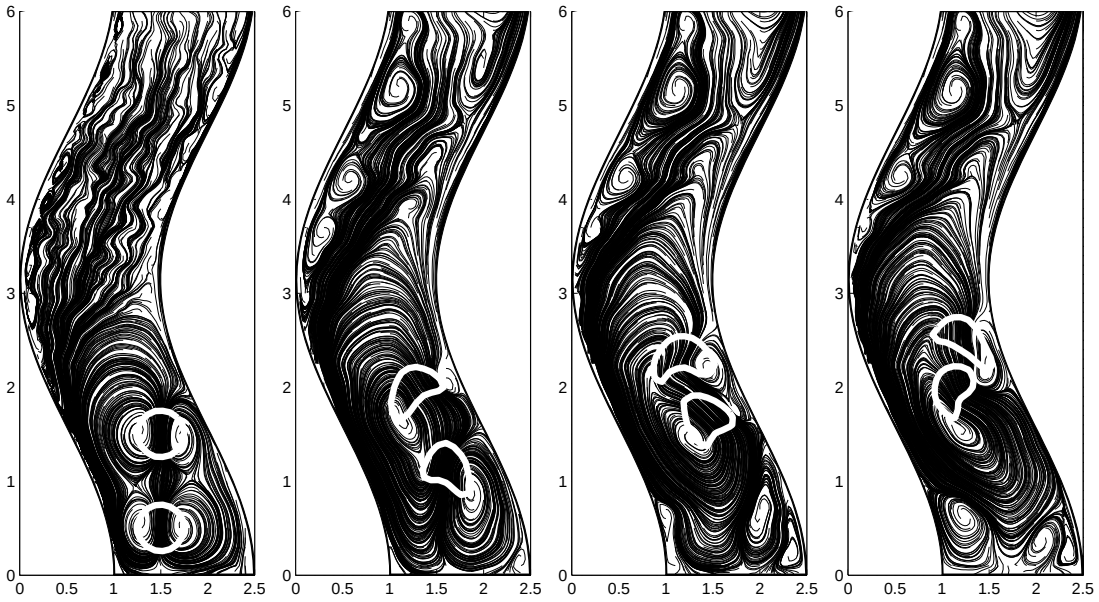

Figure 3: 1. Interaction of two bubbles in ellipsoidal shape regime. $Re = 20$, $Eo = 1.2$, $\mu_1/\mu_2 = 100$, $\rho_1/\rho_2 = 10^3$.

3.4 Bubble swarms

We considered nine bubbles in our bubble-swarm studies. The lowest and the middle 'rows' consisted of three bubbles located side by side and in upper 'row' one bubble was placed slightly above others to break the symmetry and to study how other bubbles behave in its wake. All bubbles were of the same size and the initial radius of the bubbles was 0.25. As seen in Figures 5 - 7, first, the top bubble starts to rise fast and two other bubbles in the top row start approaching each other. At the same time, the near-wall bubbles in the middle row begin to rise faster, while the center bubble rises slower. In the lowest row an opposite phenomenon is observed: the center bubble rises faster than the two other. After a short time, the center bubble in the middle row becomes strongly influenced by its 'neighbours' which have risen above it and the lowest center bubble reaches its wake. In the next moment, the center bubble in the middle row stretches in the horizontal direction and merges with the lowest center bubble. After the merger, the bubble still continues getting wider and upper bubbles' wakes cause it to form a neck-like shape and, finally, to break in the middle. At this time-point, both upper and lower bubbles have come very close to each other, but a merger does not occur when the bubbles are side by

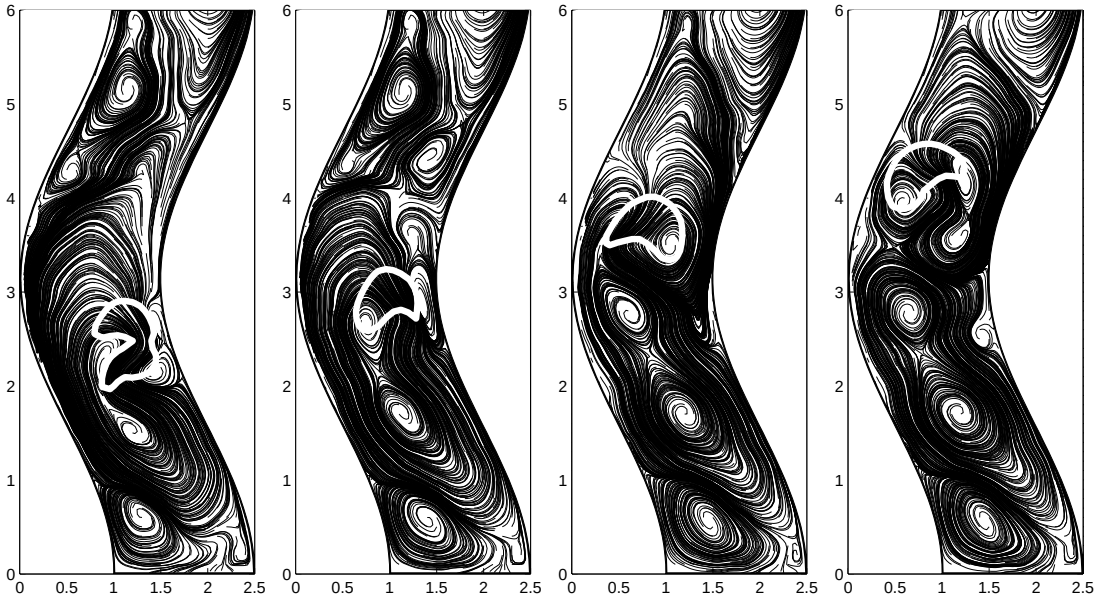

Figure 4: 2. Interaction of two bubbles in ellipsoidal shape regime. $Re = 20$, $Eo = 1.2$, $\mu_1/\mu_2 = 100$, $\rho_1/\rho_2 = 10^3$.

side: the bubbles rise steadily in groups of two (except the most upper bubble that rises alone). In [18], it is reported that 'when several bubbles were captured in the wake of another simultaneously or in a rapid sequence, they formed a cluster'. At this point of our simulation we can clearly see this effect (see Figures 5(i), 6(a),(b)). Such a type of cluster forming is also said to be 'the basic foundation for the transition from bubbly to slug flow'.

It is also noticed in [18] that 'if large number of bubbles (say $5 - 10$) were involved they formed a chimney in which a cluster's wake was strong enough to sustain itself by continually gathering in new bubbles to replace possibly dispered ones'. In our simulations, cluster of bubbles forming a chimney can be clearly seen (see Figure 6(c)). Now, the bubble groups form a wake behind them. A wake was not observed in this regime when the rise of a single bubble was studied. When the lower bubbles get closer to the upper ones, a bubble coalescence begins. First, the upper group of two bubbles merges with the 'leading' bubble and, at the same time, the group of six evolves into group of five, when two upper bubbles on the left-hand side merge together. Next, a coalescence occurs on the right-hand side of this group of five when two lowest bubble merge (see Figure 6(g) and note the non-symmetric character of the merger process). At this moment, the 'leading' bubble is reached by others; the coalescence with the 'leader' starts on the right-hand side of the bubble group (see Figures 6(h),(i) and 7(a)-(c)). This unsymmetric

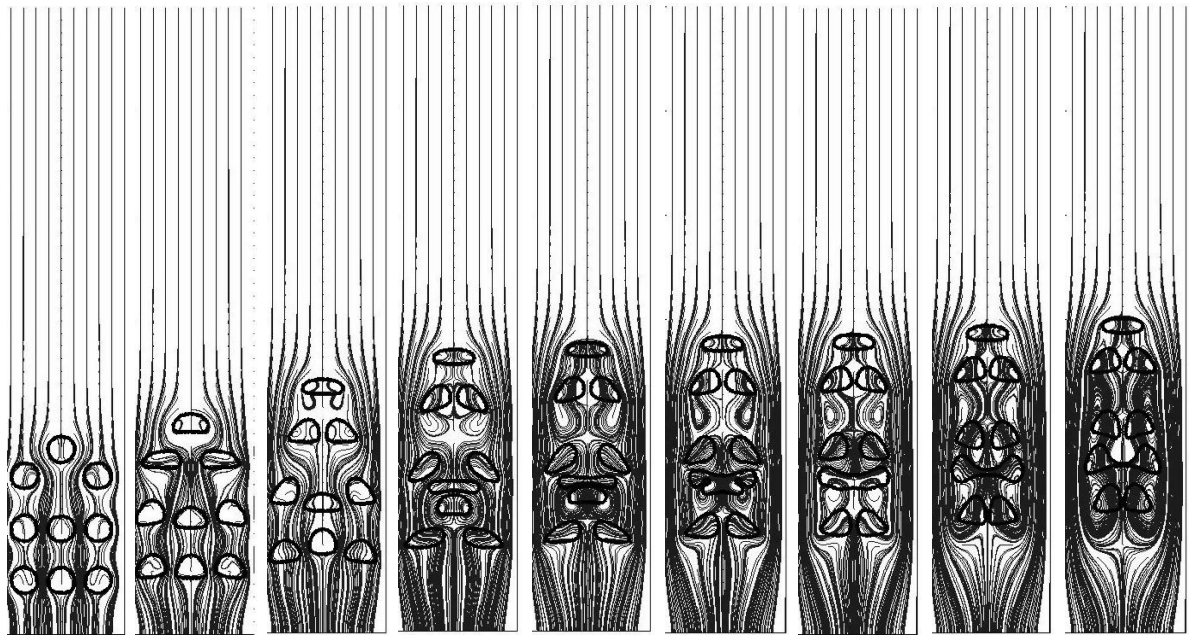

(a) (b) (c) (d) (e) (f) (g) (h) (i)

Figure 5: 1. Bubble swarm in ellipsoidal shape regime; $Re = 20$, $Eo = 1.2$, $\rho_1/\rho_2 = 10^3$, $\mu_1/\mu_2 = 10^2$.

coalescence process makes the final big bubble wobble from side to side, which, in its turn, results in an unsymmetric wake behind the bubble (and vice versa, the asymmetry of the wake causes the wobbling-type motion of the bubble, see Figures 7(d)-(h)). This kind of the bubble behaviour agrees well with the experimental studies of [18] where it is reported that '...as chimney grew stronger coalescences encouraged by the close proximity of bubbles in the cluster created large caps that greatly amplified effect...'.

Our results also compare well with the results of [19] at the point that, in some cases, the nearly uniform bubble distribution undergoes a transition to a completely different state where the bubbles accumulate in vertical streams, rising much faster than when they are uniformly distributed.

Simulations in [19] with the bubbles initially confined to a single column show that while the nearly spherical bubbles immediately disperse, the deformable bubbles stay in the column and rise much faster than uniformly distributed bubbles. This can also be seen in our simulations.

In Figure 8 one can see average velocities for bubble swarm simulations of previously presented ellipsoidal bubble swarm with four different densities. Average velocities here are simply the arithmetic means of single-bubble velocities. Figures 5 – 7 represent the simulation of the case $d_l/d_g = 1000$ that can be viewed as the fastest rising bubble-swarm. When gas density starts to grow, the average rise velocities of bubble swarms begin to

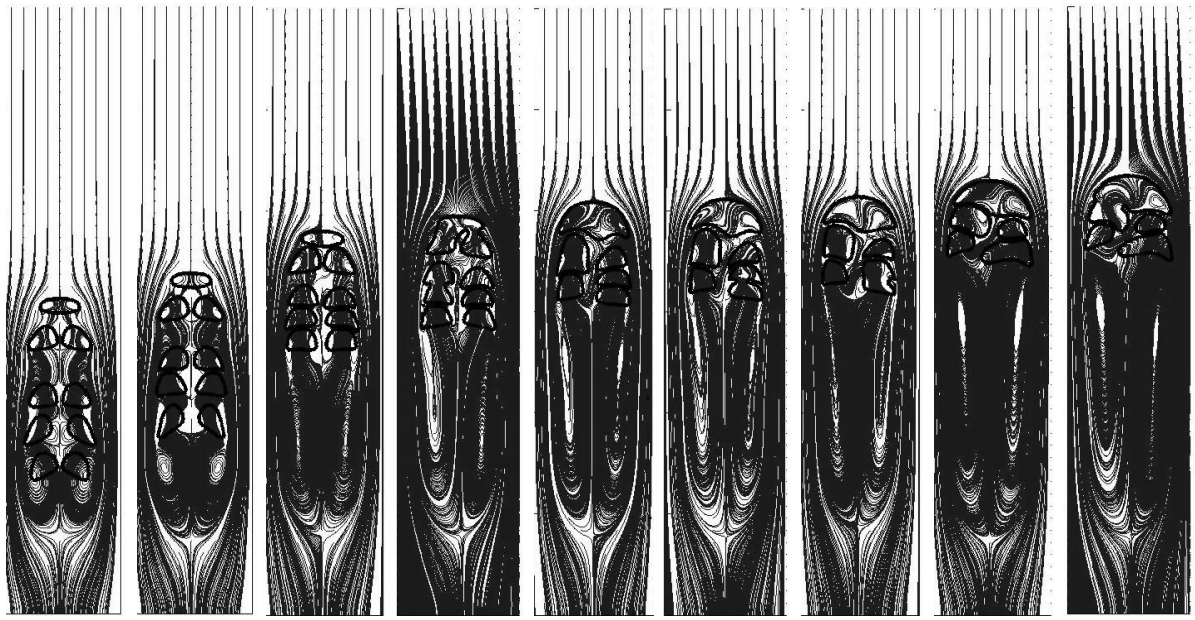

(a) (b) (c) (d) (e) (f) (g) (h) (i)

Figure 6: 2. Bubble swarm in ellipsoidal shape regime; $Re = 20$, $Eo = 1.2$, $\rho_1/\rho_2 = 10^3$, $\mu_1/\mu_2 = 10^2$.

slow down. In Figure 8, the average rise velocities grow with respect to time, which is also quite natural, since the smaller bubbles form groups and coalesce with the bigger ones.

4 CONCLUSIONS

This work is a continuation of our previous research on numerical modelling of bubble dynamics. The primary goal was to apply the existing computational method to complicated flow regimes like the wobbling-bubble rise accompanied by an intensive vortex shedding and the dynamics of a bubble swarm. It was also important to extend the method to deal with a complex geometry, in order to be able to simulate the industry-relevant problems. More results on the simulations of bubble dynamics in a complex geometry as well as the dynamics of bubble swarms will be reported elsewhere.

Acknowledgments

This work was supported by the grant 70139/98 of Tekes, the National Technology Agency of Finland. This work was also partially funded by the East Finland Universities Graduate School in Computer Science and Engineering (ECSE).

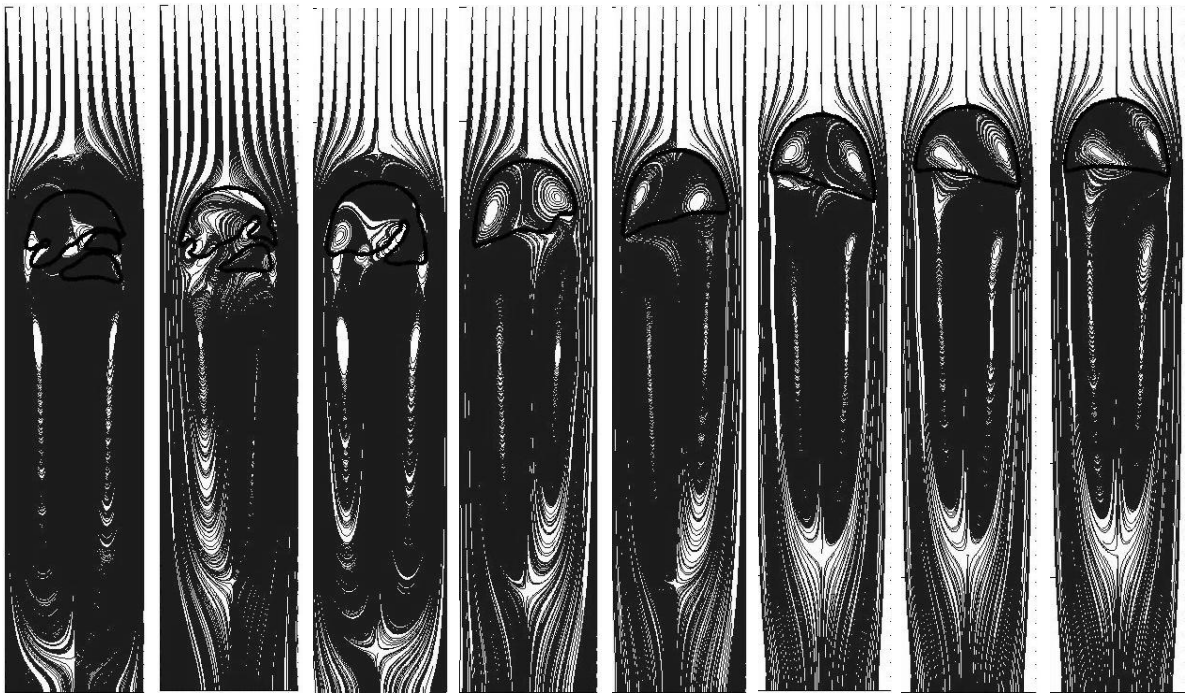

(a) (b) (c) (d) (e) (f) (g) (h)

Figure 7: 3. Bubble swarm in ellipsoidal shape regime; $Re = 20$, $Eo = 1.2$, $\rho_1/\rho_2 = 10^3$, $\mu_1/\mu_2 = 10^2$.

REFERENCES

[1] A. Smolianski, H. Haario, P. Luukka, Computational study of bubble dynamics. Submitted.

[2] A. Smolianski. *Numerical Modeling of Two-Fluid Interfacial Flows*. Ph. D. thesis, University of Jyväskylä, 2001.

[3] G.K. Batchelor. *An introduction to fluid dynamics*. Cambridge University Press, 1967.

[4] G.I. Marchuk. *Methods of numerical mathematics*. Springer, 1975.

[5] A. Quarteroni and A. Valli. *Numerical approximation of partial differential equations*. Springer-Verlag, Berlin, 1994.

[6] J.-L. Guermond and L. Quartapelle. On stability and convergence of projection methods based on pressure Poisson equation. *Int. J. Num. Meth. Fluids*, **26**, 1039-1053, 1998.

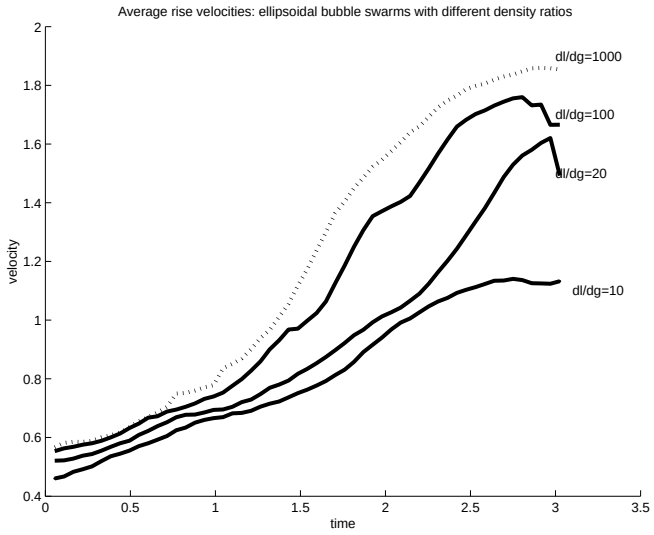

(a)

Figure 8: Average bubble-swarms rise velocities in ellipsoidal shape regime; $Re = 20$, $Eo = 1.2$, $\rho_1/\rho_2 = 10, 20, 100, 1000$, $\mu_1/\mu_2 = 10^2$.

[7] L. Quartapelle and V. Selmin. High-order Taylor-Galerkin methods for nonlinear multidimensional problems. *Finite Elements in Fluids*, Pineridge Press, 1374-1384, 1993.

[8] M. Sussman, P. Smereka and S. Osher. A level set approach for computing solutions to incompressible two-phase flow. *J. Comput. Phys.*, **114**, 146-159, 1994.

[9] S.O. Unverdi and G. Tryggvason, A front-tracking method for viscous, incompressible, multi-fluid flows. *J. Comput. Phys.*, **100**, 25-37, 1992.

[10] S. Osher and J.A. Sethian. Fronts propagating with curvature dependent speed: algorithms based on Hamilton-Jacobi formulations. *J. Comput. Phys.*, **79**, 12-49, 1988.

[11] A. J. Sethian. *Level set methods and fast marching methods: evolving interfaces in computational geometry, fluid mechanics, computer vision, and materials science.* Cambridge University Press, 1999.

[12] Y.C. Chang, T.Y. Hou, B. Merriman and S. Osher. A level set formulation of Eulerian interface capturing methods for incompressible fluid flows. *J. Comput. Phys.*, **124**, 449-464, 1996.

[13] D. Bhaga and M.E. Weber. Bubbles in viscous liquids: shapes, wakes and velocities. *J. Fluid Mech.*, **105**, 61-85, 1981.

[14] R.C. Clift, J.R. Grace and M.E. Weber. *Bubbles, drops and particles.* Academic Press, 1978.

[15] K. Tsuchiya and L.-S. Fan. Near-wake structure of a single gas bubble in a two-dimensional liquid-solid fluidized bed: vortex shedding and wake size variation. *AIChE A. Mtg, Chem. Engng. Sci.*, **43**, 1167-1181, 1988.

[16] A. Smolianski, H. Haario, P. Luukka. Numerical bubble dynamics. *Proceedings of European Symposium on Computer Aided Process Engineering ESCAPE-13*, 941-946, 2003.

[17] A Two-Dimensional Quality Mesh Generator Triangle. http://www-2.cs.cmu.edu/ quake/triangle.html (cited 12.05.2004).

[18] C.W. Stewart. Bubble interaction in low-viscosity liquids, *Int. J. of Multiphase Flow*, **21**, 1037-1046, 1995.

[19] G. Tryggvason, B. Bunner, A. Esmaeeli, D. Juric, N. Al-Rawahi, W. Tauber, J. Han, S. Nas and Y.-J. Jan. A front tracking method for the computations of multiphase flow. *J. Comput. Phys.*, **169**, 708-759, 2001.